Microstructure, water permeability and micromechanical properties of alkali activated slag subjected to accelerated leaching

Thi Nhan Nguyen, Quoc Tri Phung, Diederik Jacques, Mejdi Neji, Alexandre Dauzères, Jan Elsen, Yiannis Pontikes

To cite this version:

Thi Nhan Nguyen, Quoc Tri Phung, Diederik Jacques, Mejdi Neji, Alexandre Dauzères, et al.. Microstructure, water permeability and micromechanical properties of alkali activated slag subjected to accelerated leaching. Materials & Design, 2024, 238, pp.112706. ⟨10.1016/j.matdes.2024.112706⟩. ⟨hal-04609728⟩

HAL Id: hal-04609728
https://hal.science/hal-04609728v1

Submitted on 17 Jun 2024

Materials & Design 238 (2024) 112706

Contents lists available at ScienceDirect

Materials & Design

journal homepage: www.elsevier.com/locate/matdes

Microstructure, water permeability and micromechanical properties of alkali activated slag subjected to accelerated leaching

Thi Nhan Nguyen [a,d,*], Quoc Tri Phung [a,*], Diederik Jacques [a], Mejdi Neji [b], Alexandre Dauzeres [b], Jan Elsen [c], Yiannis Pontikes [d]

[a] *Institute for Sustainable Waste & Decommissioning, Belgian Nuclear Research Centre (SCK CEN), 2400 Mol, Belgium*
[b] *Institute of Radiation protection and Nuclear Safety (IRSN), PSE-ENV/SEDRE/LETIS, 92260 Fontenay-aux-Roses, France*
[c] *Department of Earth and Environmental Sciences, KU Leuven, 3001 Leuven, Belgium*
[d] *Department of Materials Engineering, KU Leuven, 3001 Leuven, Belgium*

ARTICLE INFO

Keywords:
Alkali activated slag
Leaching resistance
Microstructure
Permeability
Micromechanical property

ABSTRACT

This study investigated the leaching resistance of alkali activated slag mortars (AAS) under immersion in a 6 M NH_4NO_3 solution for a duration of up to 28 days, taking into consideration the effect of water-to-binder (w/b) ratio. SEM-EDS analysis revealed decalcification, desodiumization, and dealumination in AASs during leaching, leading to changes in the microstructure and micro-mechanical properties of the materials. A combination of N_2-adsorption and MIP analysis demonstrated that there was a coarsening of the structure and an increase in porosity along the depth of degradation in the leached AAS. The predominant pore framework in the leached materials was found to be capillary pores. Furthermore, the elastic modulus and micro-hardness of AAS decreased after 28 days of leaching, as evidenced by micro-indentation. The water permeability of AASs exhibited an exponential rise with the increase in porosity, both before and after leaching, as a consequence of the changes in microstructure. Notably, the w/b ratio significantly influenced the leaching rate, microstructure, and water permeability of the AAS.

1. Introduction

The lifespan of cementitious materials is potentially shortened due to ongoing leaching processes which can cause a deterioration of the materials, such as surface damage, cracking, and steel corrosion [1–4]. The direct outcome of the above is higher maintenance costs and ultimately rebuilding, as well as environmental issues [5]. In recent decades, alkali activated materials (AAMs) have emerged as promising alternative materials to conventional cement, i.e., ordinary Portland cement (OPC), because of their low CO_2 emission, good mechanical properties [6,7], and specifically better resistance to chemical attack (e.g., acid, sulfate, and chloride) [8]. The absence of portlandite, which is highly soluble (e.g., in acid or neutral pH), and the presence of a highly intense cross-linked alumino-silicate gel (C-(N)-A-S-H) diminish the penetration of external ions into the matrices of AAMs [1,9]. However, degradation/leaching of AAMs is expected during their (long-term) service life as well, depending on the application environment and the media to be in contact. For instance, AAMs would be under different acid attack if used in sewers or agriculture structures, but if used for pavement tiles, they would most likely be exposed to an urban environment. Therefore, understanding the degradation mechanism and consequent alteration in the properties of the materials is crucial. However, the leaching resistance of AAMs has not been comprehensively and systematically investigated as done for OPC [9,10]. Knowledge of the evolution of phases, microstructure, and transport properties of AAMs during leaching processes remains limited.

Because of the high pH (~13) in the pore solution of AAMs, the surrounding acidic environments can easily cause leaching and change the pH towards equilibrium. The depletion of elements, i.e., Na, K, Ca, Mg, and Al, has been observed when AAMs are exposed to different acidic solutions [9,11]. Exchange between the charge balancing cations of C-(N)-A-S-H gel (e.g., Ca^{2+} and Na^{+}) and H^{+} or H_3O^{+} from acidic solution can break the Si-O-Al bonds and finally re-organize the alumino-silicate gel structure [9,12]. It is commonly reported that the degradation of AAMs is attributed to the decalcification and dealumination of C-(N)-A-S-H gel, leading to a coarser structure after leaching. Consequently, the compressive strength decreased as observed in most studies [1], i.e., a strength loss of ~ 33 % [13] and of ~ 25 %

---

* Corresponding authors.
E-mail addresses: thi.nhan.nguyen@sckcen.be (T.N. Nguyen), quoc.tri.phung@sckcen.be (Q.T. Phung).

https://doi.org/10.1016/j.matdes.2024.112706
Received 19 September 2023; Received in revised form 13 December 2023; Accepted 24 January 2024

Table 1
Oxide composition (wt. %) of GGBFS.

Oxides	SiO_2	Al_2O_3	Fe_2O_3	CaO	MgO	K_2O	Na_2O	TiO_2	SO_3	LOI
GGBFS	32.4	11.1	0.60	43.40	7.77	0.53	0.27	1.01	2.41	0.51

[14] after exposure to CH_3COOH, and of ~ 38 % when exposed to H_2SO_4 [15]. However, the compressive strength of AASs seems to be retained from 60 days of exposure onwards, and is still much less impacted compared to the strength of OPC subjected to leaching at the same conditions. In some cases, exposing to acid can induce an alteration into other phases of AAMs and a formation of new crystalline phases which may fill the pores and consequently densify the structure [9]. However, the crystalline products can also induce cracks and expansion, depending on the content of Ca in the materials and anions of the externally attacking medium. Cracking due to the formation of crystals is profoundly observed in alkali activated slag (AAS) exposed to H_2SO_4 (>3% [16]) because of the formation of gypsum. Cracking and spalling were also observed in AAS under leaching in CH_3COOH (pH ~ 4.5) acid by Bernal *et al.* [14] and under more concentrated CH_3COOH (pH = 4.0) acid by Bakharev *et al.* [13], potentially due to the formation of a co-crystallized calcium acetate-acetic acid product ($CaH(CH_3COO)_3$) in addition to the degradation of C-A-S-H gels. A less structural deterioration, especially at the exposed surface compared to the CH_3COOH attack, localized predominantly at the exposed surface, was indicated by Shi [17] for AAS subjected to HNO_3.

Among acidic environments that OPC or AAMs can be exposed to, NH_4NO_3 solutions are commonly present at structures found in agricultural environments. In addition, leaching in 6 M NH_4NO_3 (pH ~ 4.25) is one of the most effective and popular methods to study the (long-term) durability of materials as the solution induces a similar degradation but at an increased leaching rate by two orders of magnitude compared to leaching in water for cementitious materials [18,19]. Knowledge of the performance of AAS under leaching in NH_4NO_3 solutions is limited in the literature. Komljenovic *et al.* [20] reported that no crystalline products were observed in the AASs, even up to 90-days immersion in NH_4NO_3. However, further dissolution/reaction of the slag precursor was observed during leaching, shown by a decrease in melilite and merwinite in ground granulated blast furnace slag (GGBFS) [20]. Decalcification occurs in the C-A-S-H gel of AAS during leaching, leading to a decrease in Ca/Si ratio. In contrast to a very porous structure of cementitious materials (CEM I and CEM II) upon exposure to NH_4NO_3, AASs' structure has a better resistance to leaching [8,21]. This is probably attributed to a thick protective layer of silica gel forming during the decalcification of lower-Ca C-(N)-A-S-H gels compared to C-S-H gel cements [20]. Accordingly, a slight decrease in the compressive strength of AASs was still observed after leaching [20]. Nonetheless, unlike the 81 % reduction in the compressive strength of CEM II after 60 days of leaching, a decrease of only 9 % in strength was observed for AAS [20]. Varga *et al.* [22] also presented a similar trend, indicating a less than 50 % decrease in the compressive strength of AAS after leaching compared to a 77 % decrease for OPC. To what extent the strength reduction depends on the chemical composition of precursor, w/b ratio, and activator concentration, is a largely unanswered question.

Although some studies have been performed to investigate the changes in mineralogy, C-A-S-H gel, and macro-mechanical properties of AAS under 6 M NH_4NO_3 attack [1,23,24], information on changes in the microstructure of AAS from nano to micro scale and its related physical properties (e.g., water permeability) is scarcely reported in the literature. This is surprising, considering the fact that an understanding of the microstructural evolution is crucial to estimate the leaching rate and evaluate (employing also modelling) the long-term leaching resistance of the materials. Furthermore, to the best of our knowledge, no research on the micro-mechanical properties of C-A-S-H gel after the decalcification and dealumination caused by the leaching process has been previously done. To address the knowledge gap, this study aims to investigate the changes in microstructure, elastic modulus, and water permeability of AASs under leaching in the 6 M NH_4NO_3 solution. AAS mortars with different w/b ratios are examined. Scanning electron microscope/Energy-dispersive X-ray spectroscopy (SEM/EDS), a combination of N_2 adsorption (N_2-ads) and mercury intrusion porosimetry (MIP), are used to study morphology and microstructure. Elastic modulus and microhardness of C-A-S-H gel are determined by microindentation, and water permeability is measured by using a constant flow rate [25].

Table 2
Formulation of AAS mortars.

Mortars	w/b*	SiO_2/Al_2O_3	SiO_2/Na_2O	H_2O/Na_2O
AAS 0.35	0.35	5.22	7.87	29.15
AAS 0.45	0.45	5.22	7.87	37.35
AAS 0.55	0.55	5.22	7.87	45.55

* Water in w/b ratio also includes water in activating solution. The SiO_2 and Na_2O were calculated from both GGBFS and the activator.

2. Materials and experimental setups

2.1. Materials

The commercial GGBFS used as the precursor for mortar preparation was provided by Ecocem Benelux. Its chemical composition is shown in Table 1. The GGBFS was activated by a solution made from solid NaOH pellets (99 % purity, VWR Chemicals), a commercial solid sodium disilicate supplied by VWR Chemicals (consisting of 27.5 % Na_2O, 54.5 % SiO_2, 18.0 % H_2O), and tap water. The NaOH pellets were first dissolved in distilled water to make a 10 M NaOH solution (solution A), which was cooled down before use. Sodium disilicate solution (solution B) was made by dissolving the solid sodium disilicate in a well-defined amount of water, which was calculated to reach the target w/b ratios of 0.35, 0.45, and 0.55. In this study, an activator dosage of 4.0 wt% Na_2O compared to GGBFS was used [26,27]. The solution A and B were then mixed together for 30 min to achieve a homogeneous solution (activating solution with the silicate modulus Ms = 0.45), which was cooled down to room temperature for 24 h prior to being used for activating GGBFS. Fine river sand (particle size ≤ 2 mm, with a density of 2.67 g/cm^3) was used as an aggregate (fixed 20 v/v % of mortar, which is relevant for waste immobilization application).

For the leaching test, a 6 M NH_4NO_3 solution was made from the dissolution of solid NH_4NO_3 (99.4 % purity) in deionized water. The solution was prepared at least 24 h before use to reach its equilibrium and room temperature.

2.2. Mixing procedure

Three types of AASs with different w/b ratios were prepared. Their formulations are shown in Table 2. First, GGBFS was mixed with the activating solution in a bowl for 2 min at low speed. Then, the mixing was stopped to scrap materials from the bowl wall and continued mixing afterward for 2 min more at high speed. Subsequently, sand was added, and all components were mixed for another 4 min at low speed. The fresh mortars were poured into a cylindrical polyvinylchloride (PVC) mould with an inner diameter of 97.5 mm and vibrated for 1 min to remove air bubbles inside the mortars. The moulds were then sealed and cured at 20 °C for 28 days. At 28-day curing, the cylindrical sample

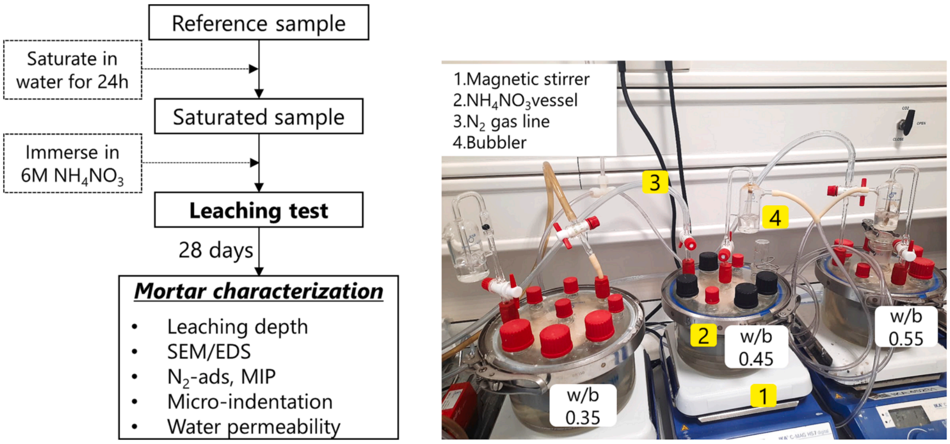

Fig. 1. Flow chart of leaching test.

together with its mould was sawn by a diamond saw into slice specimens, with a thickness of 25 mm (8 slices for each w/b ratio AAS), in which 2 slices (Reference samples) were demoulded for water permeability measurement (1 slice) and for characterization (1 slice), while the other 6 slices without demoulding were used for leaching test.

2.3. Leaching test

Each of the 6 slices for each w/b ratio-AAS was sealed by applying epoxy resin along the perimeter of the PVC ring to force unidirectional diffusion of NH_4NO_3. The slices were saturated in water at reduced pressure for 24 h before the leaching test. This saturation step aimed to avoid initial sorption or capillary forces, ensuring that the leaching process is mainly driven by diffusion [28]. Furthermore, reduced pressure was used to remove air trapped inside the samples. Although the water saturation in 24 h might cause slight leaching in AASs, this is negligible compared to the 28-day leaching of these samples in the accelerated 6 M NH_4NO_3. Then, two slices of each w/b ratio were placed in parallel in a vessel filled with 1L of NH_4NO_3 solution, corresponding to a ratio of 300 cm^2 of exposed surface area per 1L of solution. The leaching setup is shown in Fig. 1. Note that the leaching method employed in this study is an internal method, which was applied to cement [29]. Due to the complex nature of the research topic and the lack of a specific standard for AAM leaching, numerous leaching studies have been conducted using different testing procedures, such as variations in sample size, type of sample (paste, mortar, concrete), mass ratio of solution to sample, exposure duration, and solution replenishment [1]. This also applies to leaching tests in water; however, leaching in water is typically carried out over a longer period, resulting in a much higher water-to-sample ratio compared to acidic solution-to-sample ratios (e.g., 1000 vs. (4–20)) [1,30,31]. Recently, more standard documentation on leaching in acid has been published, such as ASTM 1898–20. The testing conditions used in this study are likely to be milder compared to the reported testing methods (pH ~ 4.5 and maintaining the solution throughout the entire test), which may be closer to real-world conditions. Additionally, a fast leaching rate by using NH_4NO_3 solution allows obtaining sufficiently degraded materials for characterizing at different depths and testing permeability to understand the effect of leaching on transport property alterations.

The mortar sample after 7, 14, and 28 days of leaching was taken out, cut into semicircular slices, and the leaching depth was determined by using phenolphthalein spraying (0.5 wt% in ethanol) on the fresh cutting surfaces [32]. The leaching depth (the thickness of the colorless zone) was averaged from about 20 measurements at different positions.

For mortar slices after 28 days of leaching, one slice was subjected to the water permeability test, while the other slice was cut into a 1 cm^3 cubic sample (for SEM) and into three depth layers (0–3, 3–6, and 6–9 mm from the exposed surface – for N_2-adsorption and MIP), and then freeze-dried for the characterization measurements (Fig. 2).

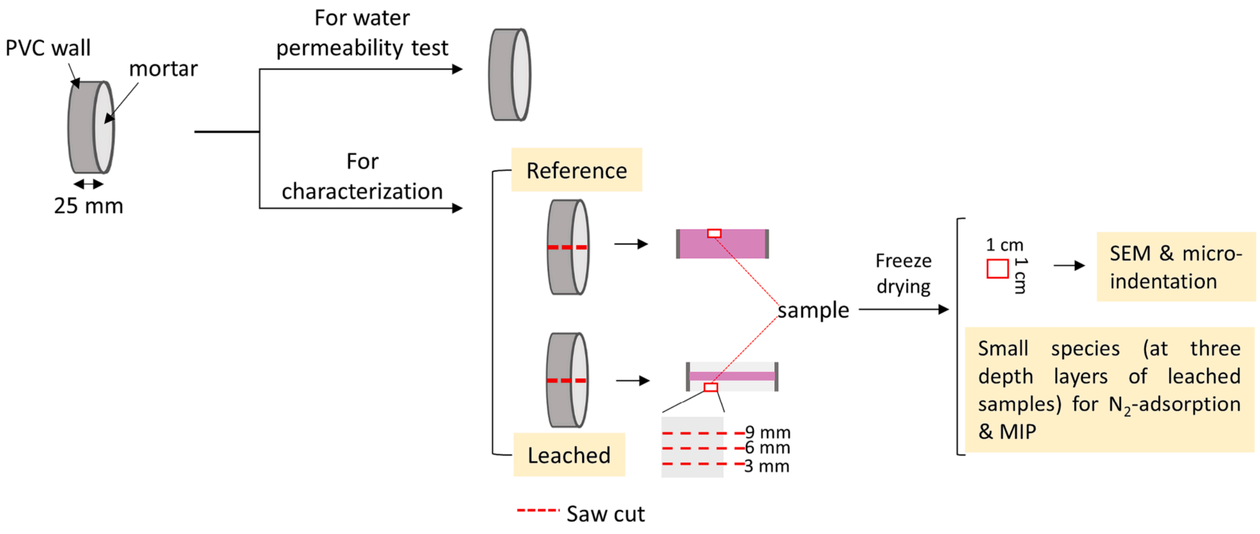

Fig. 2. Sample preparation for the permeability test and characterization.

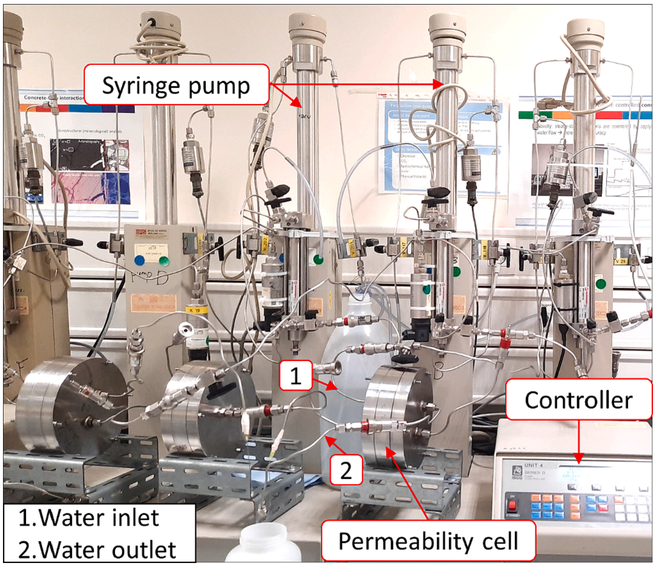

Fig. 3. Water permeability test setup.

2.4. *Water permeability*

The samples after 28 days of curing (Ref) and after 28 days of leaching (L-AAS) were used to determine water permeability by applying the controlled constant flow method [25]. The testing system, sample preparation, and testing procedure for these samples followed exactly the method described in [25]. The sample slice was embedded in a polycarbonate ring and then fixed in a permeability cell. The setup photo is shown in Fig. 3. Firstly, a pressure gradient (from 2 to 5 bar) was applied (called as the pressure mode), ensuring that the water flow rate is high enough for the measurement but not so high as to avoid cracks forming in the sample. The water flow rate was monitored until being stable. Then, the permeability test was switched to flow mode. In this mode, the value of water flow rate (the stable water flow rate obtained from the pressure mode) was set, and the pressure was recorded over a period of time. Once the difference of pressure values between two measurements was smaller than 10 % and maintained for at least 24 h, the test was considered complete. The water permeability coefficient was calculated based on the Darcy's law [33] (Eq. (1)):

$$k_w = \frac{Q \times H \times g \times \rho}{(A \times dP)} \tag{1}$$

where k_w is water permeability coefficient (m/s); Q is the rate of water flow (m^3/s); H is the thickness of sample (0.025 m); g is the gravity (9.81 m/s^2); ρ is the density of water (997 kg/m^3); A is area exposed to water (0.007462 m^2 corresponding to the diameter of 0.0975 m); dP is the average pressure gradient within 24 h (Pa).

3. Characterization

3.1. *N_2 Adsorption*

Nitrogen physisorption (N_2-ads) analyses [34] were used to determine the specific surface area and quantify the pore sizes in the range of 2–50 nm. Freeze-dried reference samples and leached samples at the three depth layers, sieved between 500 and 800 μm were measured using a TriStar 3020 device at 77 K. The specific surface area was calculated using the Brunauer–Emmett–Teller (BET) method applied to the adsorption isotherm. The pore size distribution was calculated using the Barret-Joyner-Halenda (BJH) method [35] applied to the adsorption isotherm [36]. BJH method is also recommended for the determination of pore volume in the mesopore range (2–50 nm) [37]. However, for micropores (pore width < 2 nm), the BJH method is not applied due to the uncertainty of molar volume and surface tension used in Kelvin equation [38,39]. The t-plot method is suggested to calculate the volume and surface area for such small pores instead [38].

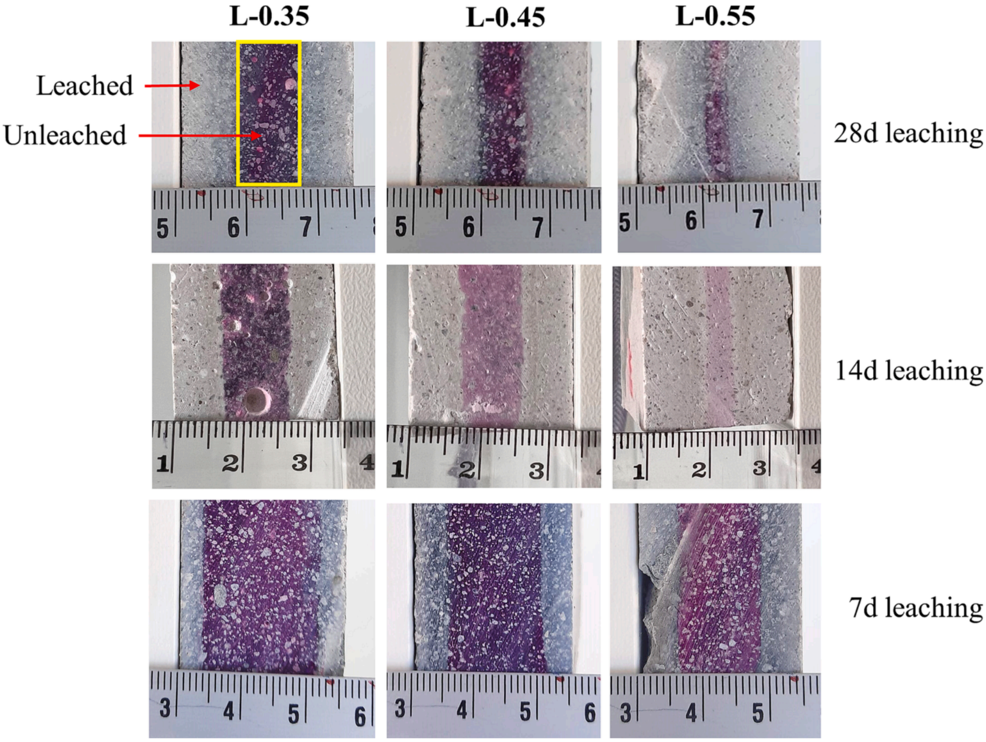

Fig. 4. Leaching depth of AASs after 7, 14, and 28 days of leaching determined by phenolphthalein spraying.

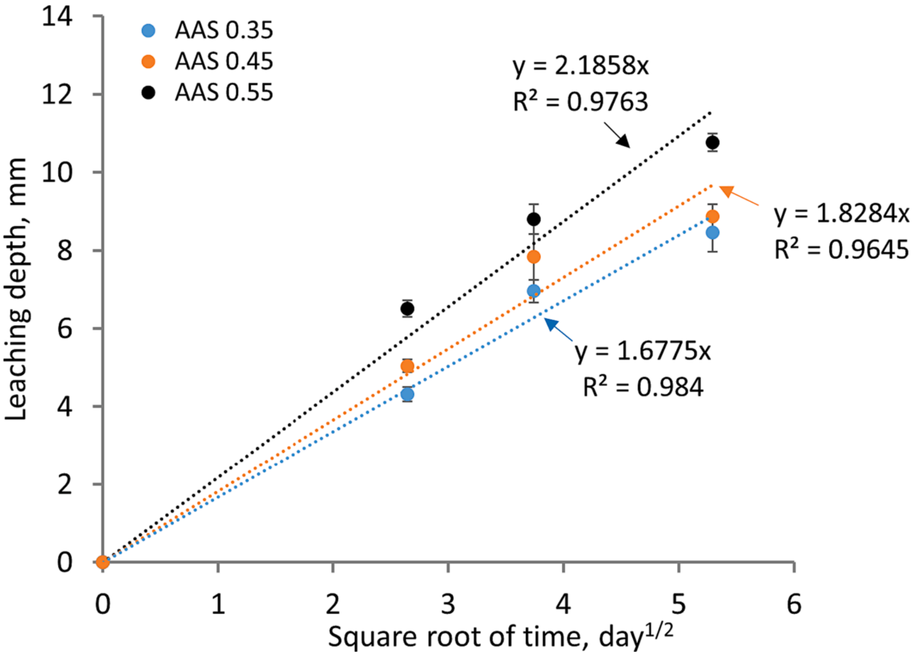

Fig. 5. Leaching depths of AASs versus the square root of leaching durations.

3.2. *Mercury instrument porosimetry*

Mercury Intrusion Porosimetry (MIP) was applied to assess the pore volume and pore size distribution of mortars in the pore size range between 0.007 and 450 μm [40]. The freeze-dried samples with a particle size of approximately 3 mm were used for MIP analysis. An AutoPore IV 9500 device, with a maximum mercury pressure of 200 MPa, was used. The pore-size distribution was calculated using the Washburn equation at a contact angle of 140° [36].

3.3. *Scanning electron microscope (SEM/EDS)*

The freeze-dried samples with a thickness of approximately 1 cm, perpendicular to the reactive surface, were analyzed with SEM imaging. These specimens were embedded in epoxy resin, polished using progressively finer sandpaper, and finally polished with diamond pastes ranging from 3 to 0.25 μm in diameter. The quality at each polishing step was monitored using an optical microscope. The surface of the specimens was then coated with gold before imaging. Backscattered electron images were recorded using a Phenom Desktop SEM at an accelerating voltage of 15 keV [36]. SEM/EDS point analyses were applied for areas within 6 mm depth from the surface of the reference and leached specimen to investigate the leaching degree of Ca, Na, and Al elements. Approximately 20 points were analyzed for each sample.

3.4. *Micro-indentation*

Targeted micro-indentation measurements were performed for the reference and 28-days leached samples with w/b of 0.35, with the focus on C-A-S-H gel areas. An Anton Paar NHT3 Nanoindenter equipped with a Berkovich diamond indenter, and a Step 700 stabilization platform was used [41]. The indentations were implemented on the surfaces of the polished samples which were also used for SEM/EDS analysis. During measurements, the displacement of the indenter and the corresponding load were recorded, which were used for calculating the elastic modulus of indented zones. The Oliver and Phar approach was applied to estimate the elastic modulus values of the indented zones [41,42]. Adapted indentation parameters were chosen in considering the roughness differences between the reference and leached materials, which could lead to unreliable elastic-modulus values. A load was first gradually increased from 0 to 100 mN with a constant loading rate of 1000 mN/s, then kept constant for 10 s at the maximum value to limit creep phenomena [41]. It was then unloaded to 0 with the same rate of 1000 mN/s.

4. Results and discussion

4.1. *Leaching rate*

The visual leaching depth of AASs after being immersed in NH_4NO_3 for 7, 14, and 18 days, using the phenolphthalein spraying method [26], is shown in Fig. 4. It is clear that the leaching depth of all samples increased over exposure time. Fig. 5 demonstrates a linear relationship between the leaching depth and the square root of exposure time, indicating a diffusion controlled leaching process [3]. The AASs with a higher w/b ratio were more susceptible to leaching. The slopes of the linear fitting lines (Fig. 5) represent the leaching rate of each AAS, and show an approximately 9 % and 30 % faster leaching when the w/b ratio increased from 0.35 to 0.45 and 0.55, respectively. The evolution of leaching depth (indicating pH of the materials' pore solution) is directly associated with the alkalinity of the pore solution. The denser pore structure of AASs with lower w/b ratios [36] might better retain a high alkalinity by diminishing the diffusion of H^+/H_3O^+ from the surrounding environment into the matrix. Phung *et al.* [3] also reported a significant increase in the degradation rate (70 %) and Ca-leaching rate (50 %) with an increase in the w/b ratio from 0.325 to 0.425 for cementitious mortars. The leaching rates of AASs seemed less influenced by the w/b ratio compared to that of cementitious materials, which is assigned to the finer pores combined with the absence of the highly soluble portlandite in the samples with the same w/b ratio [1,9]. In agreement, Bakharev *et al.* [13] indicated twice the leaching depth of cement compared to AAS concrete (5 mm) after two months of immersion in CH_3COOH ($pH = 4$), while Mellado *et al.* [43] showed a degradation depth of 1 mm and 0.8 mm for OPC and AAS pastes, respectively, after being exposed to 1 M HNO_3 ($pH = 2$) for 120 h. Under the same exposure conditions, fly ash-based geopolymer presented a higher leaching depth (1.2 mm). However, AAM pastes produced from the blend of fly ash (FA) and GGBFS illustrated a lower leaching depth

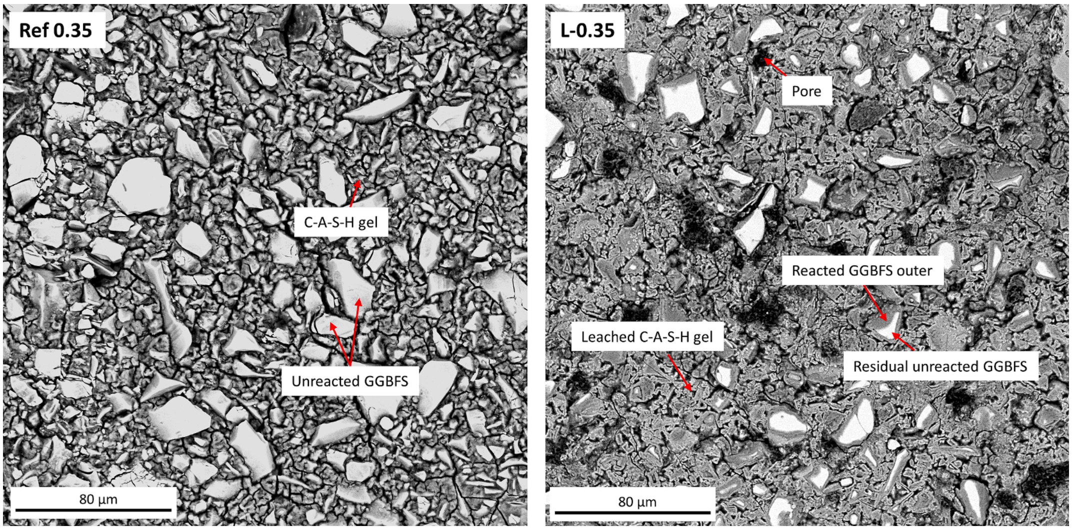

Fig. 6. SEM images (within 1 mm depth from the surface) of AAS 0.35 before (Ref) and after 28 days of leaching (L).

compared to OPC paste when attacked by acidic solutions (pH = 2–4), i.e., a 26.3 % reduction in the leaching depth of AAM (50 % FA + 50 % GGBFS) compared to that of OPC after 150d under 2-pH acid [44]. The leaching depth determined by phenolphthalein only provides a visualization of the extent of acid penetration, which strongly depends on the pore structure of the materials. However, it does not imply the degree of materials deterioration, which should be evaluated through mineralogical, structural, and mechanical properties. In addition to Ca-leaching, which causes the degradation of AAS, the leaching of Na and K also contributes to the degradation of AAS as previously indicated in [10,24,45]. Changes in the content of these elements during the leaching process were therefore determined by SEM/EDS (Section 4.2).

4.2. Morphology and leaching of Ca, Na, and Al of C-A-S-H gel

The morphologies of representative reference (Ref) and 28d-leached (L) specimens with a w/b ratio of 0.35 are shown in Fig. 6. The reference matrix was highly denser with a considerable amount of unreacted GGBFS particles surrounded by C-A-S-H gels. After leaching, the matrix appeared more porous, showing increased visual fractions of pores, as elaborated upon in Section 4.3. A further dissolution/reaction of unreacted slag might happen during the leaching evidenced by a reduction of unreacted slag amount in SEM images. Notably, the morphology of leached C-A-S-H deferred significantly from the reference gels, indicating an alteration of C-A-S-H caused by the NH_4NO_3 attack.

To have a better understanding of the alteration in C-A-S-H, atomic ratios of Ca/Si versus Na/Si and Al/Si within the gel areas of all samples before and after 28 days of leaching were quantified by EDS point analysis. These findings, illustrated in Fig. 7, present atomic ratios obtained from EDS analysis, which are regarded here as semi-quantitative results due to challenges in accurately identifying 'pure' C-A-S-H gel without potential contamination from surrounding phases. Additionally, a 2-sample *t*-test was conducted to statistically analyze the data. The primary objective was to calculate mean and standard deviation of Ca/Si and Na/Si ratios and to assess significant differences between reference and leached samples with varying w/b ratios. The detailed *t*-test results are documented in Table 3.

For the reference samples, the Ca/Si of Ref 0.35 was slightly higher than that of the mortars with a higher w/b ratio. Considering that Ca was originated only from GGBFS, the observation above suggests a higher amount of dissolved/reacted slag in the lowest w/b ratio sample. With the fixed Na_2O content (4.0 wt.% per 100 g GGBFS) for all cases, a lower water supply (lower w/b ratio) will increase the alkaline concentration and thereby promote the geopolymerization. This was also consistent with the lowest amount of remnant slag in the AAS 0.35 detected by ^{29}Si NMR in our previous study [26]. Na/Si ratios were slightly lower in reference Ref 0.35 compared to higher w/b ratio samples, consistent with the Ca/Si ratios, indicating gradual substitution of Na by Ca in C-(N)-A-S-H gel [46,47]. Higher Ca content corresponded to lower Na content in the C-(N)-A-S-H gel. Notably, Na/Si ratios in the C-(N)-A-S-H were notably higher than the designed total Na/Si ratios (~0.23) (Table 2). This discrepancy can be explained by the majority of Na content in the materials, primarily from the activating solution, being present in gel interlayers as a charge balancing ion [46], while Si content primarily originated from the silicate activator and only ~ 45 % from reacted GGBFS [26]. Al/Si ratios in the alumino-silicate gels of reference mortars remained similar, indicating a consistent gel structure among these samples, as evidenced previously [26].

After exposure to the NH_4NO_3 solution, a significant decrease was observed in both Ca/Si and Na/Si ratios, especially the latter, which is statistically confirmed by a p-value of zero for all cases (Table 2). It is noticeable that Si seemed to remain relatively stable even when AASs were exposed to 6 M NH_4NO_3 [48] solution and even under stronger acidic solutions [9]. Therefore, the reduction of these ratios indicated the decalcification and desodiumization of the C-(N)-A-S-H gels. The leaching of Ca and Na was also observed by [12,20,49]. The exchange of H_3O^+ and NH_4^+ from the surrounding environment for Ca^{2+} and Na^+ caused their leaching out of the gels. Herein, the Ca/Si ratios decreased from around 0.6 (Ref 0.35) and 0.5 (Ref 0.45 and Ref 0.55) to approximately 0.3 for all leached samples. It is worth noting that the Ca/Si ratio of approximately 0.3 in leached samples aligns with a reported stable Ca/Si ratio of the leached AAS in literature [20], suggesting that these (0–3 mm depth) materials reached maximum Ca leaching after 28 days of exposure to 6 M NH_4NO_3. The Na/Si reduced from above 0.6 to ~ 0.1 as observed in all cases. Furthermore, the exposure of AASs to the NH_4NO_3 solution also resulted in a removal of Al from C-(N)-A-S-H gels, evidenced by a slight reduction of Al/Si after leaching. The dealumination was proposed as the subsequent step of leaching process after initial ion exchange [9,45], in which Al-O-Si was potentially weakened and finally broken due to lacking charge balancing Ca^{2+} and Na^+ cations.

4.3. Alteration in nano-microstructure

4.3.1. N_2-adsorption Analysis

Fig. 8 shows the N_2 adsorption–desorption isotherms of Ref 0.35 and the corresponding 28-days leached sample at three depth layers (0–3,

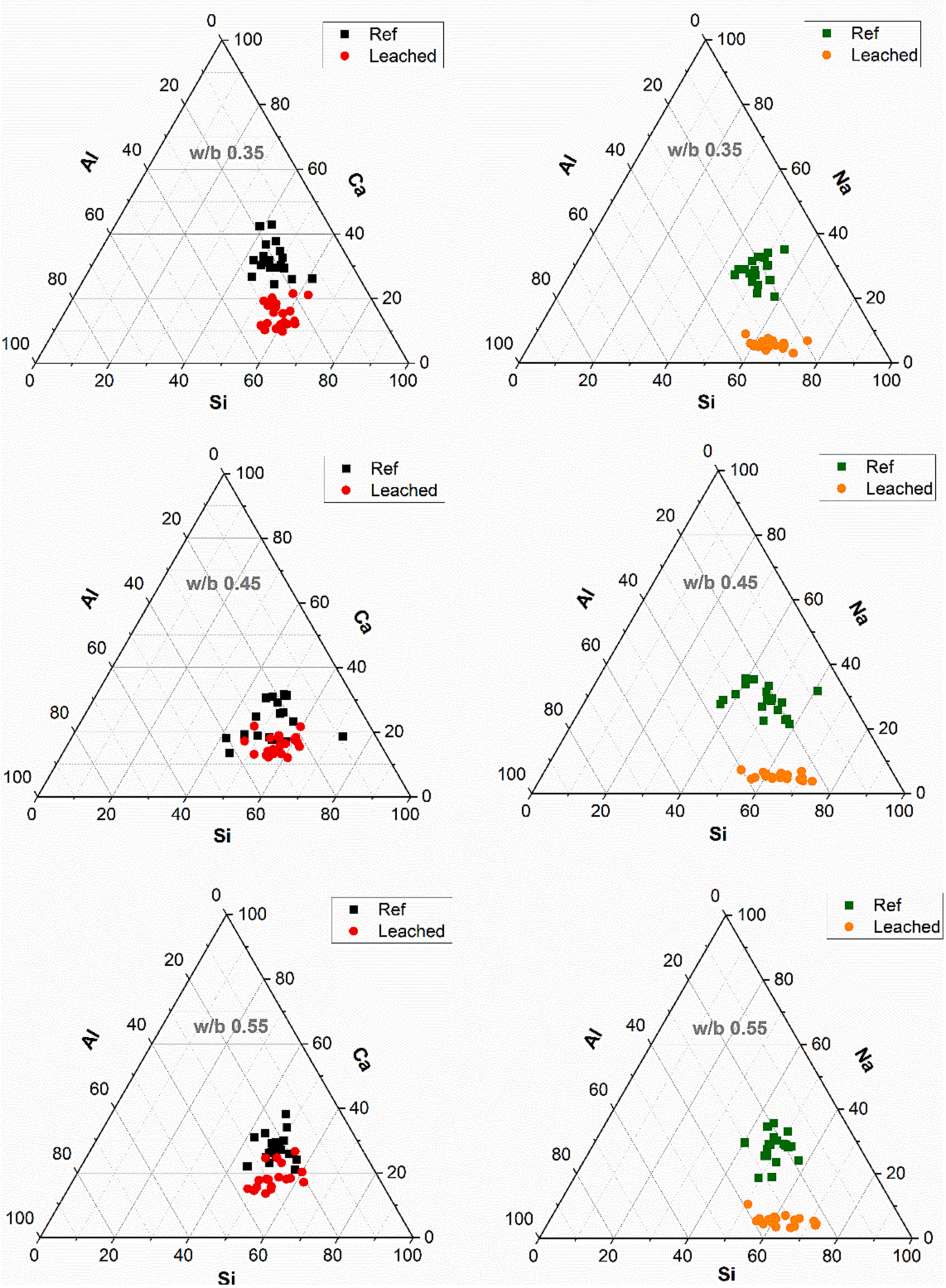

Fig. 7. Ternary diagrams of 4 major elements (Al, Si, Ca, and Na) in C-A-S-H with different ratios before (Ref) and after 28 days of leaching (Leached), obtained by semi-quantitative SEM/EDS point analysis.

Table 3

Semi-quantification of Ca/Si and Na/Si ratios in both reference and leached materials with different w/b ratios. P-values from the *t*-test are also reported to demonstrate the statistical significance of the changes in Ca/Si and Na/Si ratios due to leaching.

Molar ratio	Samples	Mean	StDev	P-value
Na/Si	Ref 0.35	0.58	0.10	0.00
	L-0.35	0.10	0.03	
	Ref 0.45	0.66	0.14	0.00
	L-0.45	0.08	0.02	
	Ref 0.55	0.62	0.11	0.00
	L-0.55	0.09	0.04	
Ca/Si	Ref 0.35	0.64	0.12	0.00
	L-0.35	0.27	0.07	
	Ref 0.45	0.50	0.12	0.00
	L-0.45	0.29	0.06	
	Ref 0.55	0.52	0.07	0.00
	L-0.55	0.34	0.07	

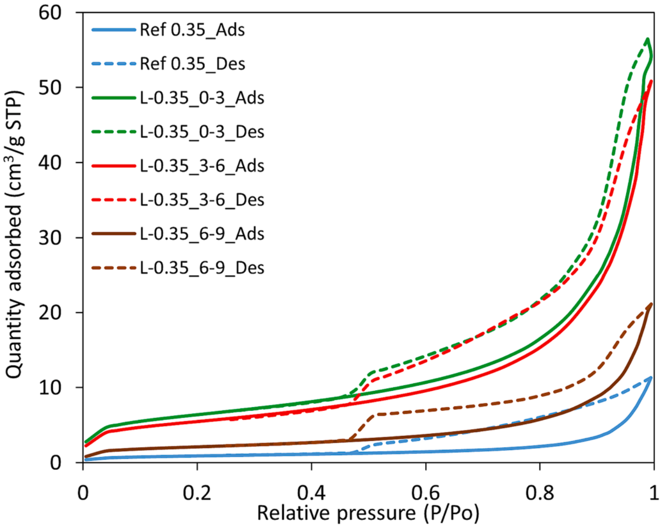

Fig. 8. Adsorption/desorption isotherms of reference 0.35 (Ref) and 28-day leached 0.35 (L) for different depth layers.

3–6, and 6–9 mm from the exposed surface). The hysteresis loops of the leached species differ from that of the reference mortar, indicating a modification of the pore structure (3–50 nm) because of leaching. In the adsorption branch, the leached layers at 0–3 and 3–6 mm absorbed a much larger quantity of nitrogen than that of the deeper layer (6–9 mm) and reference one (Ref). This implies that the pore structure was more porous after leaching. Additionally, NH_4NO_3 affected mostly within 6 mm from the exposed surface of AAS 0.35, which is consistent with its ~ 8 mm-leaching depth shown in Fig. 5. On the other hand, the desorption hysteresis of leached samples was slightly broader, especially from 0.5 to 0.7 of P/P_0, compared to that of the reference, implying narrower necks in the leached networks (ink-bottle effects) [50,51].

Changes in the cumulative pore volume and pore size distribution (PSD) of all w/b ratio AASs before and after 28d of leaching (over depth layers) are shown in Fig. 9. Furthermore, the average pore size, specific surface area (SSA), and porosity of these samples are reported in Table 4. In the nano-mesopore range (presented by BJH results), a significant increase of the pore volume (porosity) after leaching was observed in all samples. The (0–6 mm) leached layers showed a porosity of about 4, 2, and 1.5 times higher than the porosity of the reference samples with w/b ratios of 0.35, 0.45, and 0.55, respectively. In contrast, the porosities of deeper layer (6–9 mm) of leached AASs were relatively close to that of reference ones, suggesting only a slight nanostructural alteration due to leaching. Consistently, the micro porosity (<2 nm, representing the volume of gel pores [52]) witnessed a significant increase due to leaching, implying the coarsening structure of C-A-S-H gel as a result of decalcification indicated by EDS. The PSDs of leached AASs seemed smaller than that of reference samples (Fig. 9-right). Correspondingly, the average pore diameters (Table 4) witnessed a decrease after leaching in all cases. This reduction was potentially due to the opening of initially closed nano pores during leaching rather than a structural refinement, as reported by Phung *et al.* [29]. The increase in porosities combined with the decrease in pore diameters can explain the significant increase in SSA upon NH_4NO_3 attack. Up to 7, 4, and 2.5 times higher SSAs were observed for leached AASs with w/b ratios of 0.35, 0.45, and 0.55, respectively. The SSA increase was attributed to the C-(N)-A-S-H dissolution and re-organization. Indeed, the micro surface area (Table 4) showed the same trend. According to leaching depth measurements (Section 4.1), the mixtures with higher w/b ratios were leached faster (mainly related to the pH characteristics of pore solution); however, the leached matrix of the lowest w/b ratio sample was the most structurally modified. This is explained by a potentially higher volume of closed pores in the matrix of the lowest w/b ratio sample (AAS 0.35) because of its higher viscosity than the samples with higher w/b ratios [53]. These closed pores were then modified under the dissolution during leaching and consequently led to further modification of the C-(N)-A-S-H matrix.

4.3.2. *Combination of N_2-adsorption and MIP*

To investigate the influence of NH_4NO_3 attack on the AASs structure at larger pore size range (capillary up to 400 μm), MIP measurements were carried out. However, the data provided by MIP for pore diameters smaller than 0.01 μm might not be sufficiently accurate. MIP results potentially overestimated such small pore ranges because the applied high pressure during the measurements can cause structural damage [54–56], especially for leached samples. The pore structure at these small pores size assessed by N_2-ads could be more reliable than MIP. Therefore, a combination of MIP and N_2-adsorption data allows for a better evaluation of the alteration in the pore structure of AASs from gel to meso and macrospore ranges upon leaching. We followed the combination procedure proposed in [57]. The porosities obtained from the combination of reference and 28-days leached mixtures are shown in Fig. 10, in which the porosities determined by N_2-adsorption were taken in the pore ranges smaller than ~ 0.09 μm for Ref 0.35 and ~ 0.11 μm for Ref 0.45 and Ref 0.55; and ~ 0.08 μm for all leached samples to ensure continuous curves with MIP data for larger pore size ranges.

Fig. 10 presents a significant increase in porosities (in the pore size range of 0.003 – 400 μm) of reference mixtures with an increase in the w/b ratio. Approximately 2.5 and 3.5-time higher porosities were observed when the w/b ratio of reference AASs increased from 0.35 to 0.45 and 0.55, respectively. This explained the leaching rate increase with the increase of w/b ratio as discussed in section 4.1. Notably, the porosities of the reference samples were considerably smaller than that of cement with a similar w/b ratio reported in [3,24,58] (e.g., porosity of ~ 20 % in CEM IV compared to ~ 6 % in AAS with the same w/b ratio of 0.35; the porosity of ~ 20 % in CEM I with the w/b ratio of 0.425 compared to ~ 15 % in AAS with the w/b ratio of 0.45), further confirming the finer structure of the C-A-S-H network. After 28 days of leaching, porosities of the (0–3 mm) layers vastly increased, i.e., 283 %, 92 %, and 41 % for the leached samples L-0.35, L-0.45, and L-0.55 compared to that of reference samples, respectively. The porosities of deeper layers of leached samples were less affected by leaching. In particular, the porosities of layer (6–9 mm) were similar to the reference porosities.

Changes in porosities were associated with a shift in of PSDs towards larger pore size ranges (Fig. 11) due to leaching. The threshold pore diameter of reference AASs tended to shift to a bigger range with the increase in the w/b ratio but mostly remained smaller than 1 μm. Their critical pore sizes were in the gel and small capillary pore range (<0.03 μm). In contrast, the main pore distributions of leached mixtures were below a pore size of 0.1, 0.15, and 0.3 μm for the w/b ratios of 0.35,

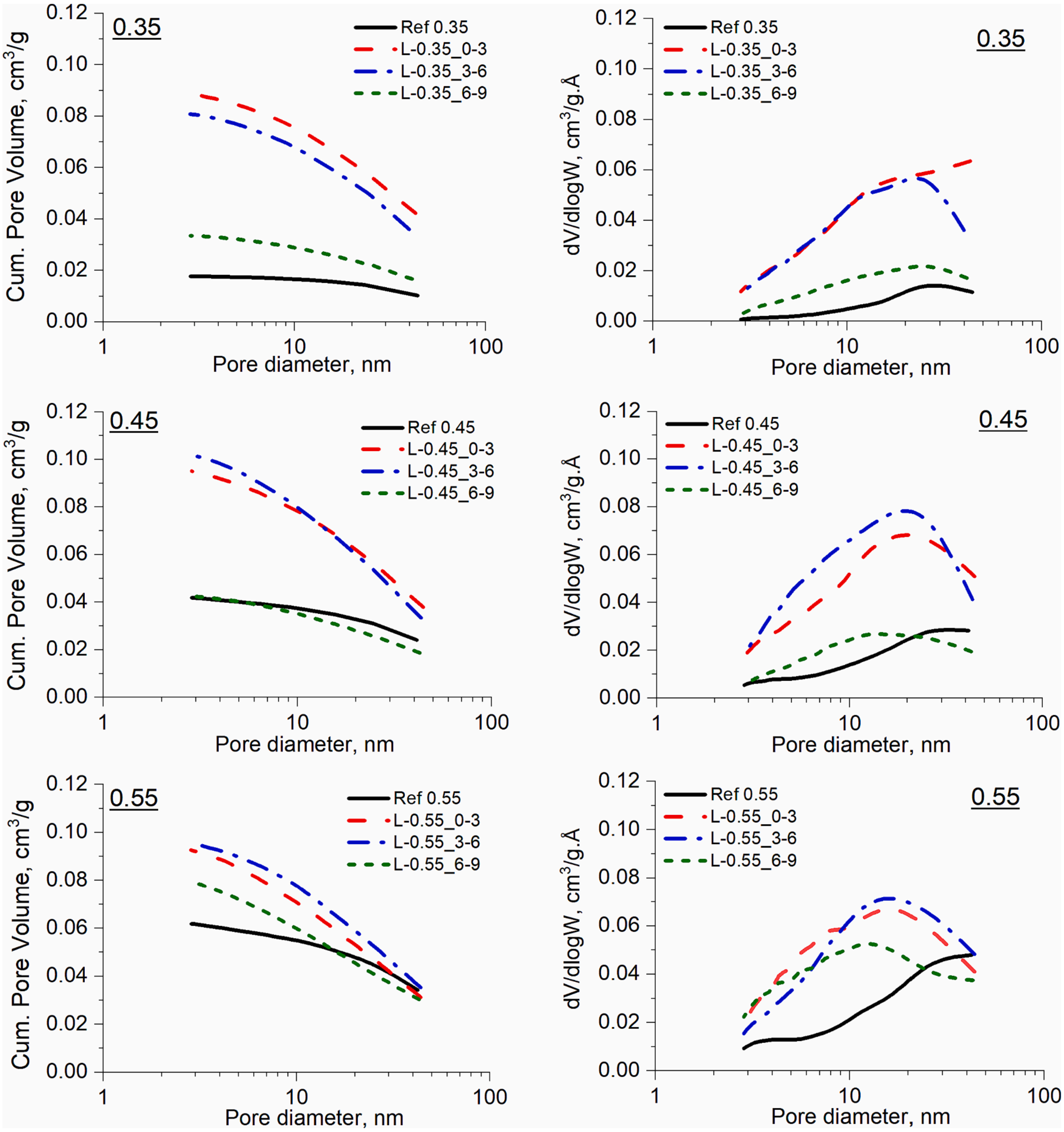

Fig. 9. Cumulative pore volume (left) and pore size distribution (right) of reference AAS (Ref) and 28d leached sample over depth profiles (up to 9 mm depth from the exposed surface), assessed by N_2 adsorption.

0.45, and 0.55, respectively. Two or three distinguished peaks were observed in the leached materials. The first peak around 0.01 μm corresponded to C-A-S-H gel, and the second (and third) peak between 0.01 and 0.1 μm belonged to small and medium capillary pores which were dominant in all leached matrices. The penetration of NH_4NO_3 into the AAS matrices caused the deterioration of Si-O-T (T: Si or Al) of C-A-S-H gel, which resulted in an increase of capillary pores and reduction of gel pores [59,60]. However, the modification of C-A-S-H gel might generate octahedral aluminate [59] which can partially fill or clog capillary pores. Therefore, the threshold sizes of leached samples were smaller than the corresponding reference ones (Fig. 11). Along degradation depths, the fraction of capillary pores and the threshold size decreased. The deeper the layer of specimens, the less porous structure. This agreed with observations of the average pore size at smaller ranges from N_2-adsorption (Table 4).

4.4. Elastic modulus and micro-hardness of C-A-S-H gel

An increase in the capillary pore fraction has been reported to influence mechanical properties [61], while a Ca/Si reduction has been linked to a decrease in the stiffness of C-S-H gel [29,62]. Therefore, we also expected an alteration in the AASs' mechanical properties due to their microstructural changes and decalcification. Targeted micro-indentation defined the micro-mechanical properties of mainly the C-A-S-H gel with the elastic modulus and micro-hardness results shown in Fig. 12 and Fig. 13, respectively. Given the heterogeneity of AAS matrix (including C-A-S-H gel, unreacted GGBFS particles, sand particles, pores, and other minor phases) and the limited resolution of scanning microscope, a carefully targeted indentation could be a viable approach to quantify the micro-mechanical properties of the main product (C-A-S-H gel) and minimize the effect of the other factors. Fig. 12 shows an average elastic modulus of around 22 GPa for the reference gel, which was higher than that of N-A-S-H gel (~17 GPa) [63] and low-density C-S-H (~18 GPa) [64]. However, the elastic modulus of C-(N)-A-S-H gel

Table 4

Nano structure of AAS before (Ref) and after 28 days of leaching (L) assessed by N_2 adsorption.

w/b ratio	ID samples	BJH adsorption average porediameter (4 V/A) (nm)	BET surface area (m^2/g)	Porosity (2–50 nm), BJH (%)	Micro surface area ($m^2//g$)	Micro porosity (<2 nm), t-plot (%)
0.35	Ref	22.71	3.25	3.40	0.09	0.002
	L-0.35_0-3	16.08	22.57	15.80	2.84	0.23
	L-0.35_3-6	15.21	19.49	14.41	2.13	0.17
	L-0.35_6-9	16.76	7.38	5.98	1.11	0.90
0.45	Ref 0.45	18.69	7.59	7.02	0.22	0.008
	L-0.45_0-3	14.48	26.43	16.06	2.45	0.19
	L-0.45_3-6	13.02	28.89	17.19	2.79	0.20
	L-0.45_6-9	15.01	10.39	7.17	1.57	0.12
0.55	Ref 0.55	18.09	12.65	10.07	0.62	0.03
	L-0.55_0-3	12.46	30.75	14.84	3.68	0.26
	L-0.55_3-6	14.05	28.86	15.26	4.21	0.31
	L-0.55_6-9	12.98	28.53	12.71	2.82	0.19

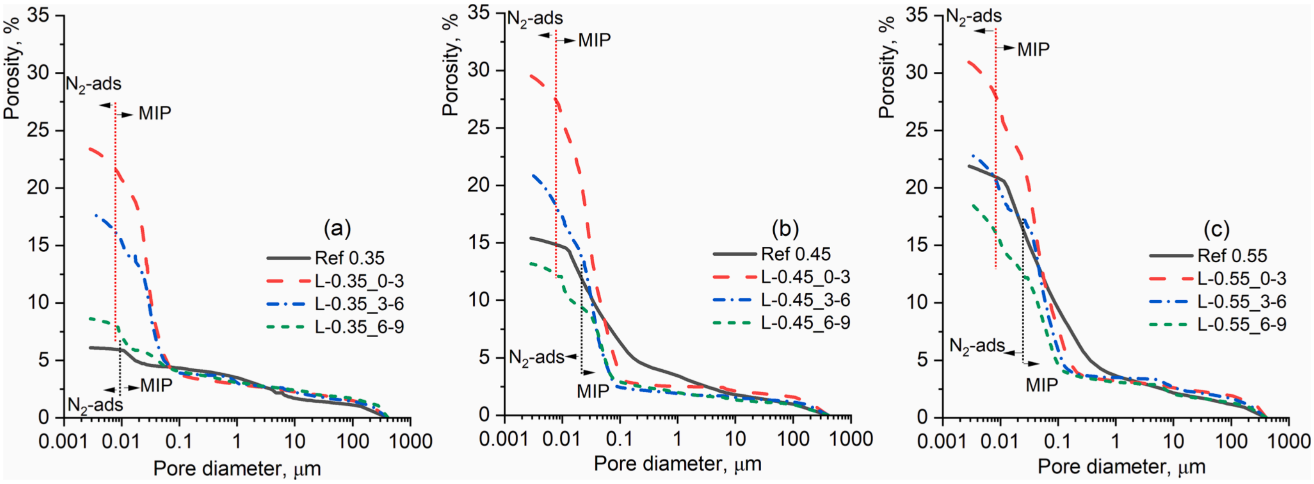

Fig. 10. Porosity of AAS mortars with w/b ratio of 0.35 (a), 0.45 (b), and 0.55 (c) before and after 28-day leaching over depth profiles.

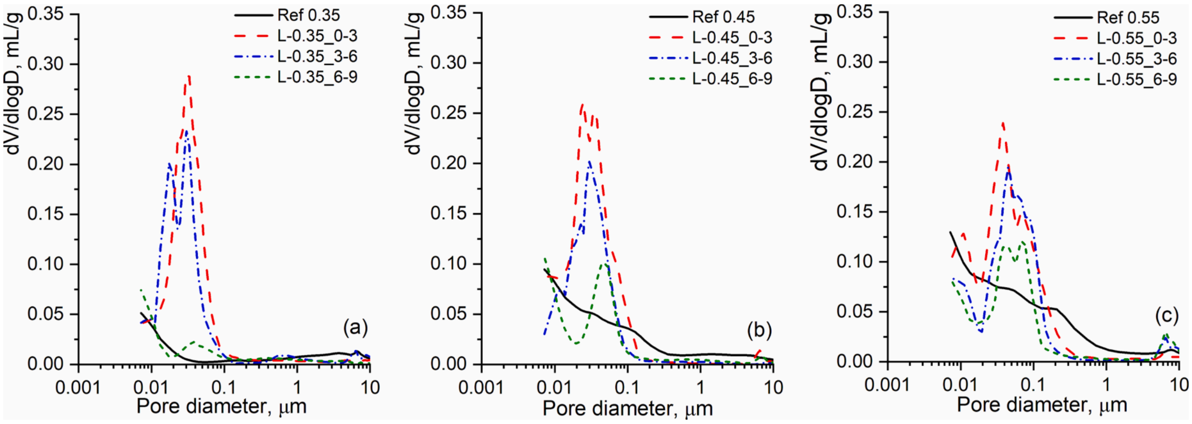

Fig. 11. Pore size distribution of AAS before (Ref) and after leaching (L) over depth profiles, assessed by MIP.

varies in a large range from ∼ 11 to 30 GPa, depending on Ca-content, silicate modulus of the activating solution, and curing time [42,63,65]. In general, the modulus of mature C-A-S-H gel (>28 days of curing) were higher than N-A-S-H gel and in range from 20 to 30 GPa [66,67], except for a few high-density cases which might reach 40 GPa [66]. After leaching, a significant decrease to ∼ 11.5 GPa (∼48 % reduction) was

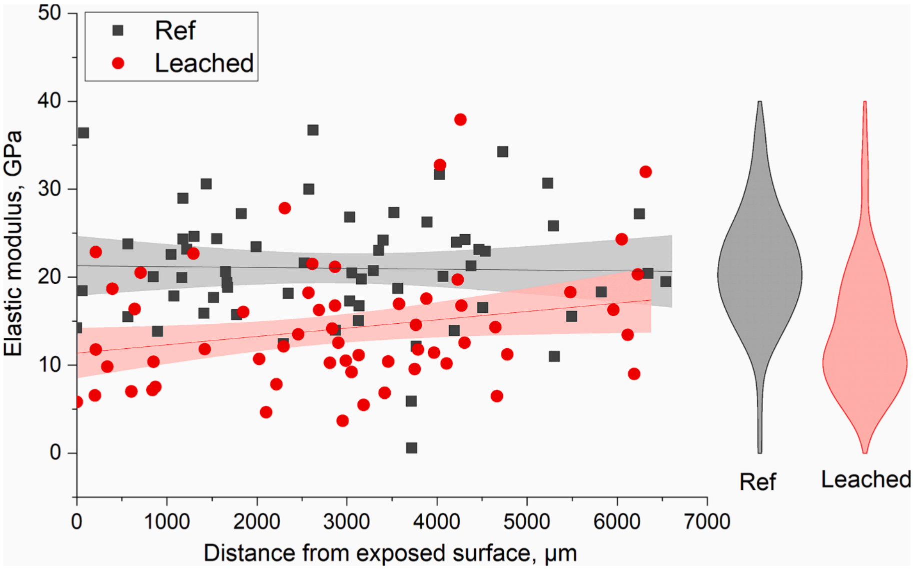

Fig. 12. Elastic modulus of C-A-S-H gel before (Ref) and after 28 days of leaching (Leached) within 6 mm depth.

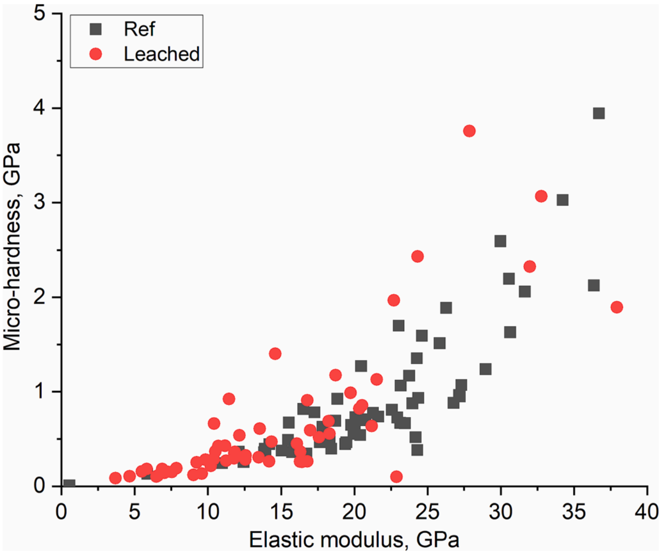

Fig. 13. Micro-hardness of C-A-S-H gel before (Ref) and after 28 days of leaching (Leached) and its correlation with elastic modulus.

observed (Fig. 12) in the gel of leached materials near the exposed surface, suggesting a reduced stiffness of the leached layer. With increasing degradation depth, the elastic modulus tended to increase and approach the value of the reference gel for materials deeper than 6 mm, which is consistent with the degradation depth of AAS 0.35 (Fig. 5). The decrease in modulus is attributed to the consequences of decalcification of C-A-S-H during leaching as indicated by SEM/EDS, leading to a profound N-A-S-H gel-like structure and a coarser network (higher porosity). In addition, leaching of Na weakened the bonds of Si-O-Al in the gel and consequently reducing the modulus. Decalcification caused by leaching in 6 M NH_4NO_3 also occurred in cement and decreased the elastic modulus of its C-S-H gel. However, a significant modulus reduction (~87 %) from 28.7 to 9.1 GPa was observed for C-S-H [68], implying a better resistance of C-A-S-H to NH_4NO_3 compared to C-S-H. In addition, the indentation defined changes in the hardness of C-A-S-H gel (Fig. 13). Generally, the leached gel had a lower hardness than the reference gel. However, there was no distinct relation between the elastic modulus and the hardness.

Table 5
Water permeability (m/s) and total porosity (%) of AASs before (Ref) and after 28d leaching.

	Ref 0.35	Ref 0.45	Ref 0.55	L-0.35	L-0.45	L-0.55
Composite permeability, m/s	4.64E-14	2.22E-13	1.12E-12	5.45E-14	4.05E-13	3.19E-12
Composite porosity, %	6.10	15.41	21.89	13.67	19.29	23.13
Leaching depth, mm	–	–	–	8.46	8.87	10.76
Porosity of leached materials, %				17.12	21.35	23.84
Permeability of leached materials, m/s				5.94E-14	6.11E-13	4.55E-12

4.5. Changes in water permeability and its correlation with porosity

The increase in the w/b ratio significantly increased the water permeability of reference AASs, e.g., approximately 5 times and 117 times higher when the w/b ratio increased from 0.35 to 0.45 and 0.55, respectively, as shown in Table 5. After 28 days of exposure to NH_4NO_3, the permeability of the samples increased by 17 %, 82 %, and 185 % corresponding to three examined w/b ratios in ascending order. This change is less pronounced compared to the changes in the permeability of CEM I (e.g., an increase of 800 %) [3], once again confirming the superior resistance of AAS to NH_4NO_3. It is worth noting that the permeability of the samples should be interpreted as a composite permeability because the sample was not fully leached (evidenced by Fig. 4). With the assumption that the permeability of the leached zone remains constant along the leaching depth, the series model introduced in [69,70] can be used to estimate the permeability of leached materials as follows:

$$k_{com} = \frac{L}{\frac{2d_l}{k_l} + \frac{L-2d_l}{k_0}} \tag{1}$$

where k_l, k_0, and k_{com} denote the permeability of leached materials, unleached (sound) materials, and the entire sample, respectively. d_l and L denote the leaching depth and the thickness of the entire sample, respectively. The calculated permeability of leached materials is

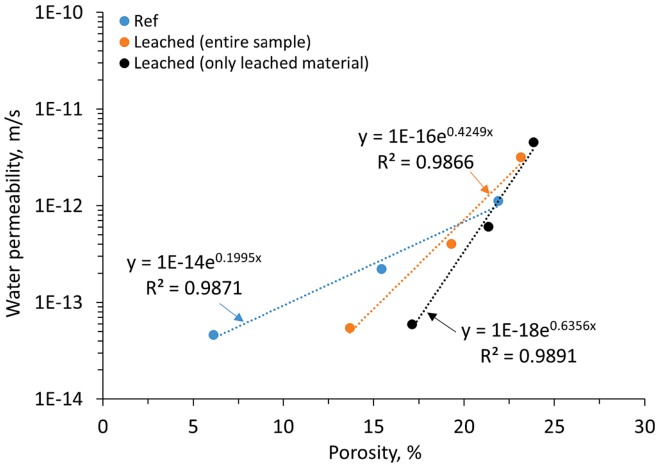

Fig. 14. Relationship between water permeability and average porosity.

reported in Table 5, with values relatively higher than the composite permeability. In comparison to reference materials, the permeability of leached materials increased by 28 %, 175 %, and 305 % for w/b ratios of 0.35, 0.45, and 0.55, respectively.

Water permeability and other transport properties are strongly affected by the microstructure of materials [3,71–73]. Therefore, the more porous AAS structure due to leaching (Section 4.3) could lead to an increase in its permeability. Fig. 14 illustrates an exponentially increasing relationship between water permeability and the total porosity of reference, composite (leached + sound) samples, and leached materials. Note that the total (composite) porosities of the leached AAS samples and the porosities of their leached parts were calculated as average values because of differences in the porosity along the depth of the leached specimen as indicated by the combination of N_2-ads and MIP. According to the leaching depth, the layers deeper than 9 mm were considered as unleached parts (sound materials); consequently, the porosity of these layers could be assigned to that of corresponding reference samples. The average porosities of leached AAS specimens and leached materials were reported in Table 5. Fig. 14 shows a more significant increase in the permeability of leached materials and leached samples with an increase in porosity, compared to the permeability of reference samples. This suggests greater complexity in the connected pore network due to leaching, thereby causing longer paths for the transport of water (typically known as the tortuosity of materials [74]). In addition, other characteristics of the pore network were potentially changed due to leaching, such as PSD, SSA, connectivity, and micro-cracks as partially observed by N_2-adsoption and MIP. Furthermore, cracks were also visually observed in SEM (Appendix 1, Fig. 15.). These parameters could also affect the permeability.

5. Conclusions

This study investigated the influence of accelerated leaching in 6 M NH_4NO_3 on the microstructure, water permeability, and micromechanical properties of AASs. In summary, the leaching process significantly coarsened the pore structure along the degradation depth, leading to an increase in water permeability and reductions in both elastic modulus and micro-hardness. Changes in these properties notably depended on the w/b ratio, which was recommended to be lower than 0.55. Further detailed conclusions and remarks are as follows:

- The leaching of AAS in a 6 M NH_4NO_3 solution followed a diffusion-controlled process, with the degradation depth increasing linearly with the square root of exposure time. A higher w/b ratio of AAS resulted in a more pronounced increase in the degradation depth. The degradation rate was approximately 9 % and 30 % faster when the w/b ratio increased from 0.35 to 0.45 and 0.55, respectively.
- Overall, the microstructure of AAS became more porous after accelerated leaching, as evidenced by an increase in total porosity, specific surface area, and a shift to the medium capillary pore range (0.01–0.3 μm) in the pore size distribution. The degree of microstructural deterioration increased along the degradation depth of immersed specimens, with the most degraded layer occurring approximately 6 mm from the exposed surfaces of AASs.
- The w/b ratios significantly affected the microstructure of AAS and its evolution during leaching. The total porosity was recorded as 2.5 and 3.5 times higher when the w/b ratio increased from 0.35 to 0.45 and 0.55, respectively, leading to faster leaching of the higher w/b ratio AASs. Notably, the completely leached part (0–3 mm depth) of the lowest w/b ratio case showed the most notable change in the microstructure compared to its reference mixture. This change was attributed to the opening of blocked pores and the reorganization of the pore network through the dissolution caused by the leaching process. However, the structure of leached AASs with a higher w/b ratio was coarser and more porous than that of those with a lower w/b ratio.
- The coarsened microstructure of AAS because of the increasing w/b ratio and immersion in the NH_4NO_3 solution resulted in an increase in water permeability. An approximately 5 times and 117 times higher permeability was observed when the w/b ratio increased from 0.35 to 0.45 and 0.55, respectively. After 28 days of leaching, the permeability of leached materials increased by 28 %, 175 %, and 305 % for the corresponding w/b ratios of 0.35, 0.45, and 0.55, respectively. Changes in water permeability correlated well with average porosity through an exponential relationship, with the permeability of leached materials being more susceptible to changes in porosity compared to that of reference AAS.
- The leaching of Ca, Na, and Al from the C-(N)-A-S-H network, as evidenced by SEM/EDS analysis, induced a coarsened microstructure. As a result, the elastic modulus of the alumino-silicate gel reduced from around 22 to 11.5 GPa after 28 days of leaching, and the hardness of the gel also exhibited a reduction due to leaching.

More information is needed on the mineralogical alteration of AAS under leaching in order to understand the underlying degradation mechanism. This study's findings on microstructure and permeability, combined with mineralogical alteration information, will aid in the development and validation of future reactive transport and geochemical models. These models will be crucial for predicting the long-term performance of AAS in 6 M NH_4NO_3. Furthermore, in order to simulate real leaching conditions, it is important to study the leaching of AAS in water and compare it to the leaching in NH_4NO_3 solution. Additionally, this study aimed to evaluate the impact of mainly NH_4NO_3 by considering that CO_2 possibly dissolved in water did not affect the results (by bubbling N_2 gas during leaching). However, it is worth noting that in reality, dissolved CO_2 can react with Ca^{2+} from decalcification to form $CaCO_3$ on the exposed surface. This could potentially affect the leaching behaviors of AAS and should be considered.

CRediT authorship contribution statement

Thi Nhan Nguyen: Conceptualization, Methodology, Data curation, Writing – original draft, Formal analysis, Investigation, Writing – review & editing. **Quoc Tri Phung:** Conceptualization, Methodology, Data curation, Writing – original draft, Supervision, Writing – review & editing. **Diederik Jacques:** Conceptualization, Supervision, Writing – review & editing. **Mejdi Neji:** Data curation, Investigation, Writing – original draft, Writing – review & editing. **Alexandre Dauzeres:** Funding acquisition, Supervision, Writing – review & editing. **Jan Elsen:** Supervision, Validation, Writing – review & editing. **Yiannis Pontikes:** Conceptualization, Supervision, Writing – original draft,

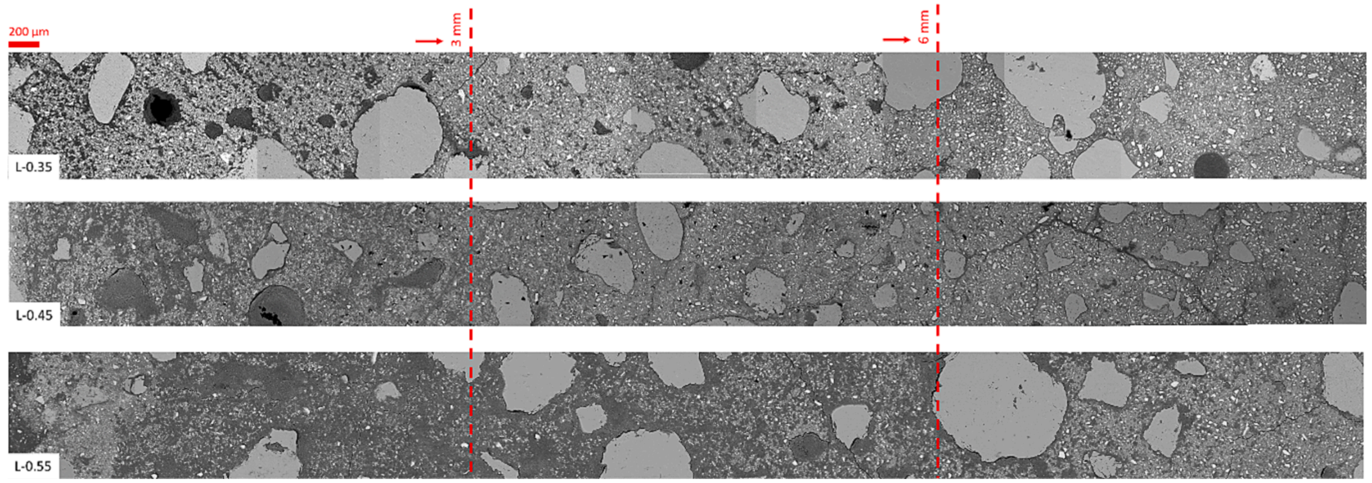

Fig. 15. Morphology (up to 9 mm depth from the exposed surface) of AASs with different w/b ratios after 28 days of leaching. The more pronounced pore fractions (gray areas) were visually observed in locations closer to the exposed surface and in the samples with higher w/b ratios. Cracks were observed in all leached matrices.

Writing – review & editing.

Declaration of competing interest

The authors declare that they have no known competing financial interests or personal relationships that could have appeared to influence the work reported in this paper.

Data availability

Data will be made available on request.

Acknowledgment

This work received funding (in part) from the Belgian Energy Transition Fund (ASOF project), IRSN (France), and the European Union's Horizon 2020 Research and Innovation Programme for Nuclear Fission and Radiation Protection Research (Call NFRP-2019-2020) under grant agreement No. 945098 (PREDIS).

Appendix 1. SEM images up to 9 mm depth from exposed surface

.

References

[1] T.A. Aiken, L. Gu, J. Kwasny, G.F. Huseien, D. McPolin, W. Sha, Acid resistance of alkali-activated binders: A review of performance, mechanisms of deterioration and testing procedures, Constr. Build. Mater. 342 (2022).

[2] C. Grengg, G.J.G. Gluth, F. Mittermayr, N. Ukrainczyk, M. Bertmer, A. Guilherme Buzanich, M. Radtke, A. Leis, M. Dietzel, Deterioration mechanism of alkali-activated materials in sulfuric acid and the influence of Cu: A micro-to-nano structural, elemental and stable isotopic multi-proxy study, Cem. Concr. Res. 142 (2021).

[3] Q.T. Phung, N. Maes, D. Jacques, J. Perko, G. De Schutter, G. Ye, Modelling the evolution of microstructure and transport properties of cement pastes under conditions of accelerated leaching, Constr. Build. Mater. 115 (2016) 179–192.

[4] D. Jacques, Q.T. Phung, J. Perko, S.C. Seetharam, N. Maes, S. Liu, L. Yu, B. Rogiers, E. Laloy, Towards a scientific-based assessment of long-term durability and performance of cementitious materials for radioactive waste conditioning and disposal, J. Nucl. Mater. 557 (2021) 153201.

[5] Y. Xie, X. Lin, T. Ji, Y. Liang, W. Pan, Comparison of corrosion resistance mechanism between ordinary Portland concrete and alkali-activated concrete subjected to biogenic sulfuric acid attack, Constr. Build. Mater. 228 (2019) 117071.

[6] J. Zhang, C. Shi, Z. Zhang, Z. Ou, Durability of alkali-activated materials in aggressive environments: A review on recent studies, Constr. Build. Mater. 152 (2017) 598–613.

[7] J.L. Provis, A. Palomo, C. Shi, Advances in understanding alkali-activated materials, Cem. Concr. Res. 78 (2015) 110–125.

[8] A. Wang, Y. Zheng, Z. Zhang, K. Liu, Y. Li, L. Shi, D. Sun, The Durability of Alkali-Activated Materials in Comparison with Ordinary Portland Cements and Concretes: A Review, Engineering (2020).

[9] G. Gluth, C. Grengg, N. Ukrainczyk, F. Mittermayr, M. Dietzel, Acid resistance of alkali-activated materials: recent advances and research needs, RILEM Technical Letters 7 (2022) 58–67.

[10] W. Zhao, Z. Fan, X. Li, L. Kong, L. Zhang, Characterization and Comparison of Corrosion Layer Microstructure between Cement Mortar and Alkali-Activated Fly Ash/Slag Mortar Exposed to Sulfuric Acid and Acetic Acid, Materials (basel) 15 (2022).

[11] Z. Sun, A. Vollpracht, H.A. van der Sloot, pH dependent leaching characterization of major and trace elements from fly ash and metakaolin geopolymers, Cem. Concr. Res. 125 (2019).

[12] Y. Wang, Y. Cao, Z. Zhang, J. Huang, P. Zhang, Y. Ma, H. Wang, Study of acidic degradation of alkali-activated materials using synthetic C-(N)-A-S-H and N-A-S-H gels, Compos. B Eng. 230 (2022).

[13] T. Bakharev, Resistance of geopolymer materials to acid attack, Cem. Concr. Res. 35 (2005) 658–670.

[14] S.A. Bernal, E.D. Rodríguez, R. Mejía de Gutiérrez, J.L. Provis, Performance of alkali-activated slag mortars exposed to acids, Journal of Sustainable Cement-Based Materials 1 (2012) 138–151.

[15] P. Sturm, G.J.G. Gluth, C. Jäger, H.J.H. Brouwers, H.C. Kühne, Sulfuric acid resistance of one-part alkali-activated mortars, Cem. Concr. Res. 109 (2018) 54–63.

[16] J. Aliques-Granero, T.M. Tognonvi, A. Tagnit-Hamou, Durability test methods and their application to AAMs: case of sulfuric-acid resistance, Mater. Struct. 50 (2016).

[17] C. Shi, Corrosion resistance of alkali-activated slag cement, Adv. Cem. Res. 15 (2003) 77–81.

[18] J.J. Chen, J.J. Thomas, H.M. Jennings, Decalcification shrinkage of cement paste, Cem. Concr. Res. 36 (2006) 801–809.

[19] M. Jebli, F. Jamin, C. Pelissou, E. Malachanne, E. Garcia-Diaz, M.S. El Youssoufi, Leaching effect on mechanical properties of cement-aggregate interface, Cem. Concr. Compos. 87 (2018) 10–19.

[20] M.M. Komljenovic, Z. Bascarevic, N. Marjanovic, V. Nikolic, Decalcification resistance of alkali-activated slag, J Hazard Mater 233–234 (2012) 112–121.

[21] Q.T. Phung, Effects of carbonation and calcium leaching on microstructure and transport properties of cement pastes. In, Ghent University, 2015.

[22] C. Varga, M.M. Alonso, R. Mejía de Gutierrez, J. Mejía, F. Puertas, Decalcification of alkali-activated slag pastes, Effect of the Chemical Composition of the Slag, Materials and Structures 48 (2014) 541–555.

[23] J. Zhang, C. Shi, Z. Zhang, X. Hu, Reaction mechanism of sulfate attack on alkali-activated slag/fly ash cements, Constr. Build. Mater. 318 (2022).

[24] S. Shagñay, I. Garcia-Lodeiro, F. Velasco, A. Bautista, M. Torres-Carrasco, Mineralogical and microstructural changes in alkali-activated and hybrid materials exposed to accelerated leaching, Journal of Building Engineering 64 (2023).

[25] Q.T. Phung, N. Maes, G. De Schutter, D. Jacques, G. Ye, Determination of water permeability of cementitious materials using a controlled constant flow method, Constr. Build. Mater. 47 (2013) 1488–1496.

[26] T.N. Nguyen, Q.T. Phung, Z. Yu, L. Frederickx, D. Jacques, D. Sakellariou, A. Dauzeres, J. Elsen, Y. Pontikes, Alteration in molecular structure of alkali activated slag with various water to binder ratios under accelerated carbonation, Sci. Rep. 12 (2022) 1–16.

[27] J.L. Provis, K. Arbi, S.A. Bernal, D. Bondar, A. Buchwald, A. Castel, S. Chithiraputhiran, M. Cyr, A. Dehghan, K. Dombrowski-Daube, A. Dubey, V. Ducman, G.J.G. Gluth, S. Nanukuttan, K. Peterson, F. Puertas, A. van Riessen, M. Torres-Carrasco, G. Ye, Y. Zuo, RILEM TC 247-DTA round robin test: mix design and reproducibility of compressive strength of alkali-activated concretes, Mater. Struct. 52 (2019).

[28] D. Bondar, Q. Ma, M. Soutsos, M. Basheer, J.L. Provis, S. Nanukuttan, Alkali activated slag concretes designed for a desired slump, strength and chloride diffusivity, Constr. Build. Mater. 190 (2018) 191–199.
[29] Q.T. Phung, N. Maes, D. Jacques, G. De Schutter, G. Ye, Investigation of the changes in microstructure and transport properties of leached cement pastes accounting for mix composition, Cem. Concr. Res. 79 (2016) 217–234.
[30] L. Diaz Caselles, B. Balsamo, V. Benavent, V. Trincal, H. Lahalle, C. Patapy, V. Montouillout, M. Cyr, Behavior of calcined clay based geopolymers under sulfuric acid attack: Meta-illite and metakaolin, Constr. Build. Mater. 363 (2023).
[31] J. Jain, N. Neithalath, Analysis of calcium leaching behavior of plain and modified cement pastes in pure water, Cem. Concr. Compos. 31 (2009) 176–185.
[32] H.A. Khan, M.S. Khan, A. Castel, J. Sunarho, Deterioration of alkali-activated mortars exposed to natural aggressive sewer environment, Constr. Build. Mater. 186 (2018) 577–597.
[33] Q.T. Phung, D. Jacques, G. De Schutter, G. Ye, Effects of W/P ratio and limestone filler on permeability of cement pastes. In: International RILEM Conference on Materials, Systems and Structures in Civil Engineering, 2016.
[34] L. Frederickx, T.N. Nguyen, Q.T. Phung, Strength and Microstructure Characteristics of Metakaolin-Based Geopolymer Mortars with High Water-to-Binder Ratios, Sustainability 14 (2022) 3141.
[35] E. Barrett, L. Joyner, P. Halenda, Pore size distribution for porous materials, J. Am. Chem. Soc. 73 (1951) 373–380.
[36] T.N. Nguyen, Physico-chemical Evolution of Geopolymers in Contact with Aggressive Environments. PhD thesis, KU Leuven (2024).
[37] K.S. Sing, Reporting physisorption data for gas/solid systems with special reference to the determination of surface area and porosity (Recommendations 1984), Pure Appl. Chem. 57 (1985) 603–619.
[38] B.C. Lippens, J. De Boer, Studies on pore systems in catalysts: V, The t Method, Journal of Catalysis 4 (1965) 319–323.
[39] Z. Zhang, G.W. Scherer, Evaluation of drying methods by nitrogen adsorption, Cem. Concr. Res. 120 (2019) 13–26.
[40] Q.T. Phung, N. Maes, S. Seetharam, Pitfalls in the use and interpretation of TGA and MIP techniques for Ca-leached cementitious materials, Mater. Des. 182 (2019).
[41] J. Pouya, M. Neji, L. De Windt, F. Péralès, A. Socié, J. Corvisier, Mineralogical Evolution and Expansion of Cement Pastes in a Sulfate-Confined Environment, Minerals 13 (2022).
[42] M. Königsberger, L. Zelaya-Lainez, O. Lahayne, B.L.A. Pichler, C. Hellmich, Nanoindentation-probed Oliver-Pharr half-spaces in alkali-activated slag-fly ash pastes: Multimethod identification of microelasticity and hardness, Mech. Adv. Mater. Struct. 29 (2021) 4878–4889.
[43] A. Mellado, M.I. Pérez-Ramos, J. Monzó, M.V. Borrachero, J. Payá, Resistance to acid attack of alkali-activated binders: Simple new techniques to measure susceptibility, Constr. Build. Mater. 150 (2017) 355–366.
[44] J. Ren, L. Zhang, R. San Nicolas, Degradation process of alkali-activated slag/fly ash and Portland cement-based pastes exposed to phosphoric acid, Constr. Build. Mater. 232 (2020).
[45] W. Zhang, X. Yao, T. Yang, Z. Zhang, The degradation mechanisms of alkali-activated fly ash/slag blend cements exposed to sulphuric acid, Constr. Build. Mater. 186 (2018) 1177–1187.
[46] C. Liu, X. Liang, Y. Chen, Z. Li, G. Ye, Degradation of alkali-activated slag subjected to water immersion, Cem. Concr. Compos. (2023).
[47] B. Walkley, R. San Nicolas, M.-A. Sani, G.J. Rees, J.V. Hanna, J.S.J. van Deventer, J.L. Provis, Phase evolution of C-(N)-A-S-H/N-A-S-H gel blends investigated via alkali-activation of synthetic calcium aluminosilicate precursors, Cem. Concr. Res. 89 (2016) 120–135.
[48] Z. Baščarević, M. Komljenović, Z. Miladinović, V. Nikolić, N. Marjanović, Z. Žujović, R. Petrović, Effects of the concentrated NH4NO3 solution on mechanical properties and structure of the fly ash based geopolymers, Constr. Build. Mater. 41 (2013) 570–579.
[49] M. Yang, Y. Zheng, X. Li, X. Yang, F. Rao, L. Zhong, Durability of alkali-activated materials with different C-S–H and N-A-S-H gels in acid and alkaline environment, J. Mater. Res. Technol. 16 (2022) 619–630.
[50] H. Ye, A. Radlińska, Shrinkage mechanisms of alkali-activated slag, Cem. Concr. Res. 88 (2016) 126–135.
[51] H. Ranaivomanana, J. Verdier, A. Sellier, X. Bourbon, Toward a better comprehension and modeling of hysteresis cycles in the water sorption–desorption process for cement based materials, Cem. Concr. Res. 41 (2011) 817–827.
[52] Y. Ma, G. Wang, G. Ye, J. Hu, A comparative study on the pore structure of alkali-activated fly ash evaluated by mercury intrusion porosimetry, N2 adsorption and image analysis, J. Mater. Sci. 53 (2018) 5958–5972.
[53] F. Oshani, A. Allahverdi, A. Kargari, R. Norouzbeigi, N.M. Mahmoodi, Effect of preparation parameters on properties of metakaolin-based geopolymer activated by silica fume- sodium hydroxide alkaline blend, Journal of Building Engineering 60 (2022).
[54] R. Feldman, Pore structure damage in blended cements caused by mercury intrusion, J. Am. Ceram. Soc. 67 (1984) 30–33.
[55] Y. Zuo, G. Ye, Pore Structure Characterization of Sodium Hydroxide Activated Slag Using Mercury Intrusion Porosimetry, Nitrogen Adsorption, and Image Analysis, Materials (basel) 11 (2018).
[56] F. Moro, H. Bohni, Ink-bottle effect in mercury intrusion porosimetry of cement-based materials, J Colloid Interface Sci 246 (2002) 135–149.
[57] Q.T. Phung, N. Maes, D. Jacques, Application of Multiple Techniques to Quantify Pore Structure of Degraded Cementitious Materials, in: G.D. Schutter, N.D. Belie, A. Janssens, N.V.D. Bossche (Eds.), XIV DBMC 14th International Conference on Durability of Building Materials and Components, RILEM Publications S.A.R.L, Ghent, Belgium, 2017, p. 12.
[58] Q.T. Phung, N. Maes, E. Jacops, D. Jacques, G. De Schutter, G. Ye, Insights and issues on the correlation between diffusion and microstructure of saturated cement pastes, Cem. Concr. Compos. 96 (2019) 106–117.
[59] S. Siddique, J.G. Jang, Acid and sulfate resistance of seawater based alkali activated fly ash: A sustainable and durable approach, Constr. Build. Mater. 281 (2021).
[60] A. Allahverdi, F. Skvara, Nitric acid attack on hardened paste of geopolymeric cements, Part 1, Ceramics Silikaty 45 (2001) 81–88.
[61] A. Runci, J. Provis, M. Serdar, Microstructure as a key parameter for understanding chloride ingress in alkali-activated mortars, Cem. Concr. Compos. 134 (2022).
[62] G. Constantinides, F.-J. Ulm, The effect of two types of C-S-H on the elasticity of cement-based materials: Results from nanoindentation and micromechanical modeling, Cem. Concr. Res. 34 (2004) 67–80.
[63] J. Němeček, V. Šmilauer, L. Kopecký, Nanoindentation characteristics of alkali-activated aluminosilicate materials, Cem. Concr. Compos. 33 (2011) 163–170.
[64] G. Constantinides, F.-J. Ulm, The effect of two types of CSH on the elasticity of cement-based materials: Results from nanoindentation and micromechanical modeling, Cem. Concr. Res. 34 (2004) 67–80.
[65] Y. Ma, G. Ye, J. Hu, Micro-mechanical properties of alkali-activated fly ash evaluated by nanoindentation, Constr. Build. Mater. 147 (2017) 407–416.
[66] M.R. Ahmad, C.S. Das, M. Khan, J.-G. Dai, Development of low-carbon alkali-activated materials solely activated by flue gas residues (FGR) waste from incineration plants, J. Clean. Prod. 397 (2023).
[67] R. Caron, R.A. Patel, A. Bogner, F. Dehn, Multi-scale experimental investigation and analytical micro-mechanical modeling to determine Young's modulus of alkali-activated slag concrete, Constr. Build. Mater. 383 (2023).
[68] L. Brown, P.G. Allison, F. Sanchez, Use of nanoindentation phase characterization and homogenization to estimate the elastic modulus of heterogeneously decalcified cement pastes, Mater. Des. 142 (2018) 308–318.
[69] Q.T. Phung, N. Maes, D. Jacques, G. De Schutter, G. Ye, J. Perko, Modelling the carbonation of cement pastes under a CO2 pressure gradient considering both diffusive and convective transport, Constr. Build. Mater. 114 (2016) 333–351.
[70] S. Benbow, C. Watson, D. Savage, Investigating conceptual models for physical property couplings in solid solution models of cement, in, Swedish Nuclear Power Inspectorate (2005).
[71] T.N. Nguyen, Q.T. Phung, J. Jacques, J. Elsen, Y. Pontikes, Permeability and sorptivity of alkali activated Fe-rich slag mortars. In, 8th, International Slag Valorisation Symposium, Mechelen, Belgium, 2023.
[72] Y. Ma, J. Hu, G. Ye, The pore structure and permeability of alkali activated fly ash, Fuel 104 (2013) 771–780.
[73] J. Wongpa, K. Kiattikomol, C. Jaturapitakkul, P. Chindaprasirt, Compressive strength, modulus of elasticity, and water permeability of inorganic polymer concrete, Materials & Design 31 (2010) 4748–4754.
[74] E. Jacops, Q.T. Phung, L. Frederickx, S. Levasseur, Diffusive Transport of Dissolved Gases in Potential Concretes for Nuclear Waste Disposal, Sustainability 13 (2021).